**Cite this article**
Yimit H, Zhang D, Luo Q *et al.*
Investigation of deformation coordination between optical fibre and borehole sand backfill.
*Proceedings of the Institution of Civil Engineers – Geotechnical Engineering*,
https://doi.org/10.1680/jgeen.23.00055

**Research Article**
**Paper 2300055**
Received 13/04/2023;
Accepted 31/07/2023;
First published online 03/08/2023



Geotechnical Engineering

# Investigation of deformation coordination between optical fibre and borehole sand backfill

**Hasanjan Yimit** MSc
Graduate student, School of Earth Sciences and Engineering, Nanjing University, Nanjing, P. R. China (Orcid:0000-0002-8565-3064)

**Dan Zhang** PhD
Professor, School of Earth Sciences and Engineering, Nanjing University, Nanjing, P. R. China; Key Laboratory of Earth Fissures Geological Disaster, Ministry of Natural Resources, Nanjing University, Nanjing, P. R. China (corresponding author: zhangdan@nju.edu.cn)

**Qi Luo** MSc
Graduate student, School of Earth Sciences and Engineering, Nanjing University, Nanjing, P. R. China

**Xulong Gong** PhD
Professor, Key Laboratory of Earth Fissures Geological Disaster, Ministry of Natural Resources, Nanjing University, Nanjing, P. R. China

**Haoyu Wang** MSc
Graduate student, School of Earth Sciences and Engineering, Nanjing University, Nanjing, China

**Haiyang Liao** MSc
Graduate student, School of Earth Sciences and Engineering, Nanjing University, Nanjing, P. R. China

**Land subsidence has threatened the safety of municipal infrastructures and even that of inhabitants. As one of the deformation monitoring methods, distributed optical fibre sensing (DOFS) technology has been developed for the investigation of land subsidence. The deformation coordination between the optical fibre and soil ($DC_{f\text{-}s}$) under different conditions is critical for land subsidence monitoring with DOFS. In this paper, a medium-sized triaxial apparatus was modified for testing the $DC_{f\text{-}s}$. Consolidated drained triaxial tests were conducted to investigate the effect of sand types on the $DC_{f\text{-}s}$. By linearly fitting the deformation of the sensing cable with that of the triaxial specimen, the other factors that affect the $DC_{f\text{-}s}$, such as the confining pressure, dry or wet state of the soil and cyclic variation of the loads, can be discussed. The experiments reveal that better $DC_{f\text{-}s}$ comes with a larger particle size, poor gradation of sand and larger confining pressure. The $DC_{f\text{-}s}$ of wet sand is better than that of dry sand. The $DC_{f\text{-}s}$ coefficient tends to be stable with an increase of loading cycles. The $DC_{f\text{-}s}$ obtained and its dependence on influencing factors can be used to modify the measured cable strain in practical land subsidence monitoring with DOFS.**

**Keywords:** deformation coordination/laboratory tests/optical fibre/sands/subsidence

## Notation

| | |
|---|---|
| $C_T$ | temperature coefficient |
| $C_\varepsilon$ | strain coefficient |
| $C_c$ | coefficient of curvature |
| $C_u$ | coefficient of uniformity |
| $DC_{f\text{-}s}$ | deformation coordination between optical fibre and soil |
| $D_r$ | relative density |
| $d$ | sampling interval of optical frequency domain reflectometer |
| $d_f$ | deformation integrated by strains of optical fibre |
| $d_s$ | axial deformation of specimen obtained by linear variable differential transducer |
| $E_c$ | Young's modulus of the fibre coating |
| $E_g$ | Young's modulus of the fibre core |
| $e_{max}$ | maximum void ratio |
| $e_{min}$ | minimum void ratio |
| $G_s$ | specific gravity |
| $K_0$ | coefficient of lateral earth pressure |
| $L$ | half of the specimen height |
| $l_c$ | critical adherence length |
| $r_c$ | radius of the fibre coating |
| $r_g$ | radius of the fibre core |
| $r_m$ | radius of the soil mass |
| $\alpha$ | fibre–soil strain transfer rate |
| $\Delta v_R$ | spectral shift |
| $\Delta T$ | fibre temperature change |
| $\varepsilon$ | fibre strain |
| $\bar{\varepsilon_f}$ | average fibre strain |
| $\varepsilon(i)$ | strain of the specimen measured by the optical sensing cable |
| $\eta$ | strain ratio of the sensing cable and specimen |
| $\mu$ | Poisson's ratio of the fibre core |

## 1. Introduction

Land subsidence (LS) is an environmental geological phenomenon that is defined as the gentle or rapid sinking of the ground surface (Galloway and Burbey, 2011; Wu *et al.*, 2008). It is caused by natural processes of the vertical motion of land (tectonics, glacial isostatic, sediment compaction, etc.) and anthropogenic processes (fluid extraction, construction of underground structures, etc.); LS is therefore a global threat (Shirzaei *et al.*, 2021; Xu *et al.*, 2012). More than 95 cities in China and 45 states in the USA suffer from LS and LS-induced geohazards (Bagheri-Gavkosh *et al.*, 2021; Wu *et al.*, 2008), leaving cities' pipelines and other underground

infrastructures damaged (Wang *et al.*, 2019). LS is a gradual process and a potentially destructive hazard. The cumulative potential subsidence area amounts to 2.2 million km$^2$, affecting 1.2 billion inhabitants and 21% of the global gross domestic product (GDP) (Herrera-García *et al.*, 2021). Therefore, it is necessary to monitor LS and take related preventative actions to avoid damage.

Various ground-based (e.g. differential levelling, global positioning system (GPS), tripod light detection and ranging (Lidar) and extensometry) and remote sensing (interferometric synthetic aperture radar (Insar), airborne Lidar) methods are applied to measure, monitor and map LS at local and regional scales (Bagheri-Gavkosh *et al.*, 2021; Galloway and Burbey, 2011; Wang *et al.*, 2019). In addition to the methods mentioned above, distributed optical fibre sensing (DOFS) has the advantages of long-term durability, high stability, small size and immunity to electronic interference, which make it ideal for long-term monitoring of LS (Barrias *et al.*, 2016; Leung *et al.*, 2015). As an emerging LS monitoring technology (Liu *et al.*, 2022; Zhang *et al.*, 2018), one of the critical issues is the deformation coordination between an optical fibre and the soil, to ensure accurate measurement of the soil strain distribution by using a sensing cable. The characteristics of the strain transfer to the sensing fibre have been studied theoretically and experimentally (Ansari and Yuan, 1998; Her and Huang, 2011; Yuan *et al.*, 2001). It can be deduced that reliable and effective monitoring in LS depends on the structure of the sensing cable, borehole backfill, installation depth and so on. A pull-out test on the sensing cable was adopted to examine strain/stress transfer at the fibre–soil interface (Chen and Zhang, 2011; Zhang *et al.*, 2015). The sensing cable is in a non-uniform tensile strain state in the pull-out test, and the largest strains could reach tens of thousands to hundreds of thousands of microstrains (Zhang *et al.*, 2018). In addition, the soil deforms passively in the pull-out test, and thus the deformation of the soil is no larger than that of the sensing cable. However, the soil is usually compressed for LS, and the embedded optical sensing cable will be in a compressive state accordingly. Moreover, although the ground surface deformation may be large in LS, the deformation of sand is small in every single stratum, up to thousands of microstrains (Wu *et al.*, 2015). It can be deduced that the pull-out test may not be applicable to illustrate the deformation coordination between the optical fibre and soil for the compressed sand in LS.

Based on a triaxial compression test, Wu *et al.* (2022) investigated the deformation coordination between the sensing cable and soil and developed a theoretical model of the deformation coordination between the optical fibre and the soil. A single-mode sensing cable with a diameter of 2 mm was embedded at the centre of small triaxial testing specimens, which were made of an intermediate sand of Fujian and silty clay. The bottom area and the height of the specimen were 30.6 cm$^2$ and 11.6 cm, respectively.

In this paper, a triaxial test with a larger specimen size was conducted to reduce the size effects so that a large-diameter sensing cable could be tested. A 5 mm dia. metal-reinforced cable (Ø 5 mm MRC), which is more applicable for in situ monitoring of LS, was tested. The deformation coordination between the Ø 5 mm MRC and different types of sands is presented, and the key effecting factors are examined. The results of this paper can be used for strain correction in practical LS monitoring under similar conditions.

## 2. Materials and methods

### 2.1 Optical frequency domain reflectometer-based soil strain monitoring

The optical frequency domain reflectometer (OFDR) – a high-resolution strain-sensing technology with a centimetre-scale spatial resolution over hundreds of metres and with a precision of 1 με and 0.1°C (Henault *et al.*, 2011) – was developed based on the Rayleigh scattering phenomenon. As shown in Figure 1, the incident light, a highly coherent continuous wave laser with a linear sweep frequency, is divided into two parts by an isolator. One is used as the reference light and the other is used as the detecting light that is emitted into the optical fibre. Backscattered light is generated as the detecting light travels through the optical fibre and is then mixed with the reflected reference light. The coherent interference is picked up by the photodetector, and the spectral shift is then determined (Wu *et al.*, 2020). The relation between the spectral shift and the changes in strain and temperature can be retrieved by (Henault *et al.*, 2011)

$$\Delta\nu_R = C_\varepsilon \varepsilon + C_T \Delta T \quad (1)$$

where $\Delta\nu_R$ is the spectral shift, $\varepsilon$ *is* the fibre strain, $\Delta T$ is the fibre temperature change, and $C_\varepsilon$ and $C_T$ are the strain and temperature coefficients. The fibre core used in this paper is a standard single-mode fibre. The values of $C_\varepsilon$ and $C_T$ are −0.15 GHz/με and −1.25 GHz/°C, respectively (Henault *et al.*, 2011). As the tests were carried out at a constant room temperature, it is not necessary to conduct temperature compensation.

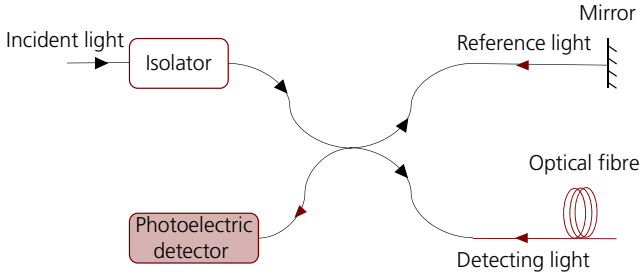


**Figure 1.** Principle of optical frequency domain reflectometer (OFDR)

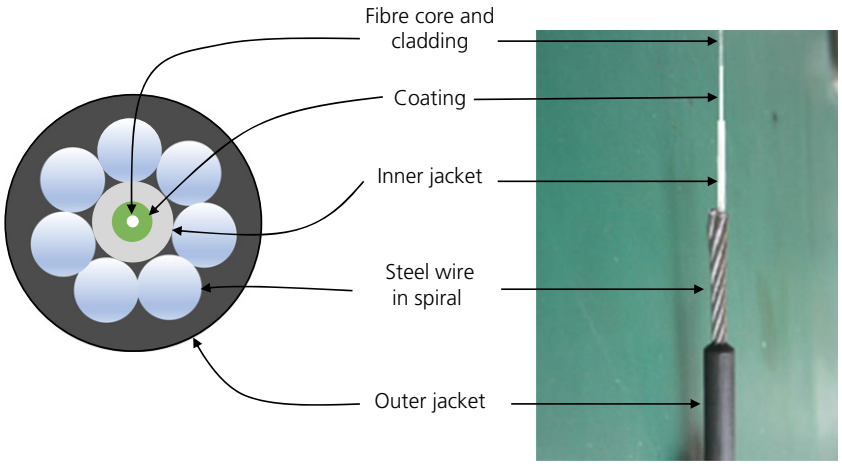


**Figure 2.** Structure of sensing cable

In this study, the strain distribution of the tested soil was directly measured using a sensing cable buried at the centre of the cylindrical specimen. The average strain of the specimen is calculated according to Equation 2

$$\bar{\varepsilon}_{\mathrm{f}} = \frac{\int_{-L}^{L} \varepsilon(l)\mathrm{d}l}{2L} = \frac{\sum_{1}^{2L/d} [\varepsilon(i) + \varepsilon(i+1)]d}{4L}$$

where $L$ is half of the specimen height, $\varepsilon(i)$ is the strain of the specimen measured by the optical sensing cable and $d$ is the sampling interval of OFDR (Wu *et al.*, 2022).

The strains of the sensing cable at both ends of the specimen are significantly less than the strains of the soil because of the end effect. According to the theoretical models of the mechanics of bond and interface shear transfer in optical fibre sensors (Ansari and Yuan, 1998; Li *et al.*, 2012), the strain ratio of the sensing cable and specimen ($\eta$) reaches its maximum (0.8–1) at the mid-point and gradually decreases (to 0, theoretically) toward both ends. Li *et al.* (2012) proposed the concept of the critical adherence length $l_{\mathrm{c}}$ (CAL), which is defined as the required minimum adherence length of the sensing cable to ensure $\eta \geq 0.9$ in at least half of the total adhered length, as shown in Equation 3. Since the calculated value of CAL for the Ø 5 mm MRC employed in this study is 90.78 mm, the measured strains in the middle one-third length of the specimen are used to obtain the soil deformation.

$$3. \quad \eta = 1 - \frac{\cosh(kl_{\mathrm{c}}/2)}{\cosh(kl_{\mathrm{c}})} \geqslant 0.9$$

where $l_{\mathrm{c}}$ is the CAL and $k = ((1+\mu)(E_{\mathrm{g}}/E_{\mathrm{c}})r_{\mathrm{g}}2\ln(r_{\mathrm{m}}/r_{\mathrm{g}}))^{-1/2}$, in which $E_{\mathrm{g}}$ and $E_{\mathrm{c}}$ is the Young's modulus of the fibre core and the coating; $\mu$ is the Poisson's ratio of the fibre core; and $r_{\mathrm{g}}$, $r_{\mathrm{c}}$ and $r_{\mathrm{m}}$ is the radius of the fibre core, coating and soil mass, respectively.

**Table 1.** Main properties of the sensing cable

| Layer | Material | Outer diameter: mm | Young's modulus: MPa |
|---|---|---|---|
| Fibre core and cladding | Ge-doped glass | 0.125 | 72 000 |
| Coating | Acrylate | 0.25 | 2.55 |
| Inner jacket | Hytrel | 0.9 | 15 |
| Steel wire in spiral | Stainless steel | 1.9 | — |
| Outer jacket | Polyethylene | 5 | 1070 |

## 3. Test set-up

### 3.1 Sensing cable and specimens

Sensing cables with complex sheath structures and high rigidity are generally used to cope with harsh environments in engineering monitoring. Unlike the Ø 2 mm sensing cable used in previous triaxial compression tests (Wu *et al.*, 2022), in this paper, testing was carried out on a Ø 5 mm MRC, which is widely used in LS monitoring. The structure of the sensing cable is shown in Figure 2. The Young's modulus of the sensing cable is 10.96 GPa, and the other parameters are shown in Table 1.

Three kinds of sands that can be employed as borehole backfills in LS monitoring were tested to examine the deformation relationship between the sand and the sensing cable: (*a*) filling sand (FS) – poorly graded and with the finest particle size in this test; (*b*) intermediate sand (IS) of Fujian – poorly graded; and (*c*) International Organization for Standardization standard sand (SS) of China – uniform silica sand consisting of subrounded grains with over 96% quartz (Yang *et al.*, 2009). The basic properties of the sands are given in Table 2. The particle size distribution is shown in Figure 3.

Table 2. Physical and mechanical properties of the test sands

| Sand | Specific gravity, $G_s$ | Effective particle size, $D_{10}$: mm | $D_{60}$: mm | Uniformity coefficient, $C_u$ | Curvature coefficient, $C_c$ | Gradation | Friction angle: degrees | Minimum void ratio, $e_{min}$ | Maximum void ratio, $e_{max}$ | Relative density, $D_r$ |
|---|---|---|---|---|---|---|---|---|---|---|
| FS | 2.59 | 0.3 | 0.44 | 1.45 | 0.91 | Poorly graded | 24.37 | 1.53 | 1.96 | 0.48 |
| IS | 2.46 | 0.38 | 0.73 | 1.9 | 1.33 | Poorly graded | 25.47 | 1.31 | 1.86 | 0.61 |
| SS | 2.67 | 0.17 | 0.88 | 5.27 | 0.67 | Well graded | 25.64 | 1.41 | 1.91 | 0.52 |

### 3.2 Triaxial apparatus for deformation coordination between the optical fibre and soil analysis

A triaxial apparatus was developed to study the deformation coordination between the optical fibre and soil ($DC_{f\text{-}s}$) under the compressed state of the soil (Figures 4 and 5). The apparatus has the following features. (*a*) The triaxial test cell is 620 mm high and 306 mm in diameter, and the specimen size is $300 \times 150$ mm. A large-sized specimen is suitable for the test of Ø 5 mm MRC, which is the most commonly used sensing cable in LS monitoring (Wu *et al*., 2015). (*b*) A hole through which the sensing cable passes was drilled at the centre of the pedestal, loading cab, porous stone and filter paper so that a sensing cable can be installed through the central axis of the cylindrical specimen.

### 3.3 Test scheme and procedures

A consolidated drained (CD) test on the dry specimen was carried out first, and then a cyclic triaxial test on the wet specimen was conducted after wetting by applying a hydraulic head. The test process undergone by a specimen is shown in Figure 6. There were three loading–unloading processes in a cyclic test. The test schemes are shown in Tables 3 and 4. The maximum deviator stress was designed to be 50% of the confining pressure to avoid the specimen being destroyed. The height and diameter of the specimen were measured before installing the triaxial cell. The water content of the infiltrated specimen was measured after the cyclic CD test.

The test procedures were similar to a typical triaxial test. Some key procedures can be described as follows. (*a*) The sensing cable was passed through the hole and kept stretched during specimen preparation to achieve accurate and reliable measurements. (*b*) The split mould was dismantled after applying a small vacuum pressure in the specimen (approximately −20 kPa) that kept the shape of the specimen unchanged. (*c*) O-rings were used to ensure that the specimen was sealed where the optical cable entered and exited the specimen at both ends. (*d*) One end of the sensing cable was connected to an OFDR demodulator to collect the strain distribution. The main test procedures are shown in Figure 7.

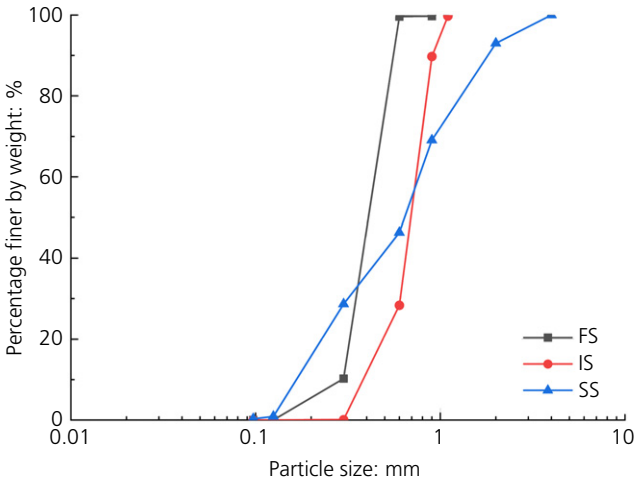


Figure 3. Particle size distribution of the soils

## 4. Experimental results and discussion

### 4.1 Strain distributions of the optical fibre

#### 4.1.1 Results of the CD test on dry sand

The shape and the changing trends of the fibre strain distributions under confining pressures of 200, 400 and 500 kPa are consistent. The strain distributions at a 400 kPa confining pressure are shown in Figure 8. The strain distributions of $FS_d$, $IS_d$ and $SS_d$ are similar. The magnitude of the strains in the specimen height direction is not uniform but basically symmetrical. The optical fibre strain is large in the middle of the specimen and gradually decreases towards both ends. However, there are some positive strains at both ends of the specimen under an unloading test condition, as most strains are negative to indicate the compression state of the specimen. This is attributed to relative slippage between the fibre optic cable and the soil. It is also evident that the optical fibre strains are proportional to the deviatoric stress. The magnitude of the optical fibre strain is not identical between the loading and unloading conditions. The strain in the loading process is smaller than that in the unloading process for the same deviatoric stress, which indicates that the optical fibre can measure the plastic deformation in the specimen. This phenomenon of plastic deformation can be confirmed by the deformation of

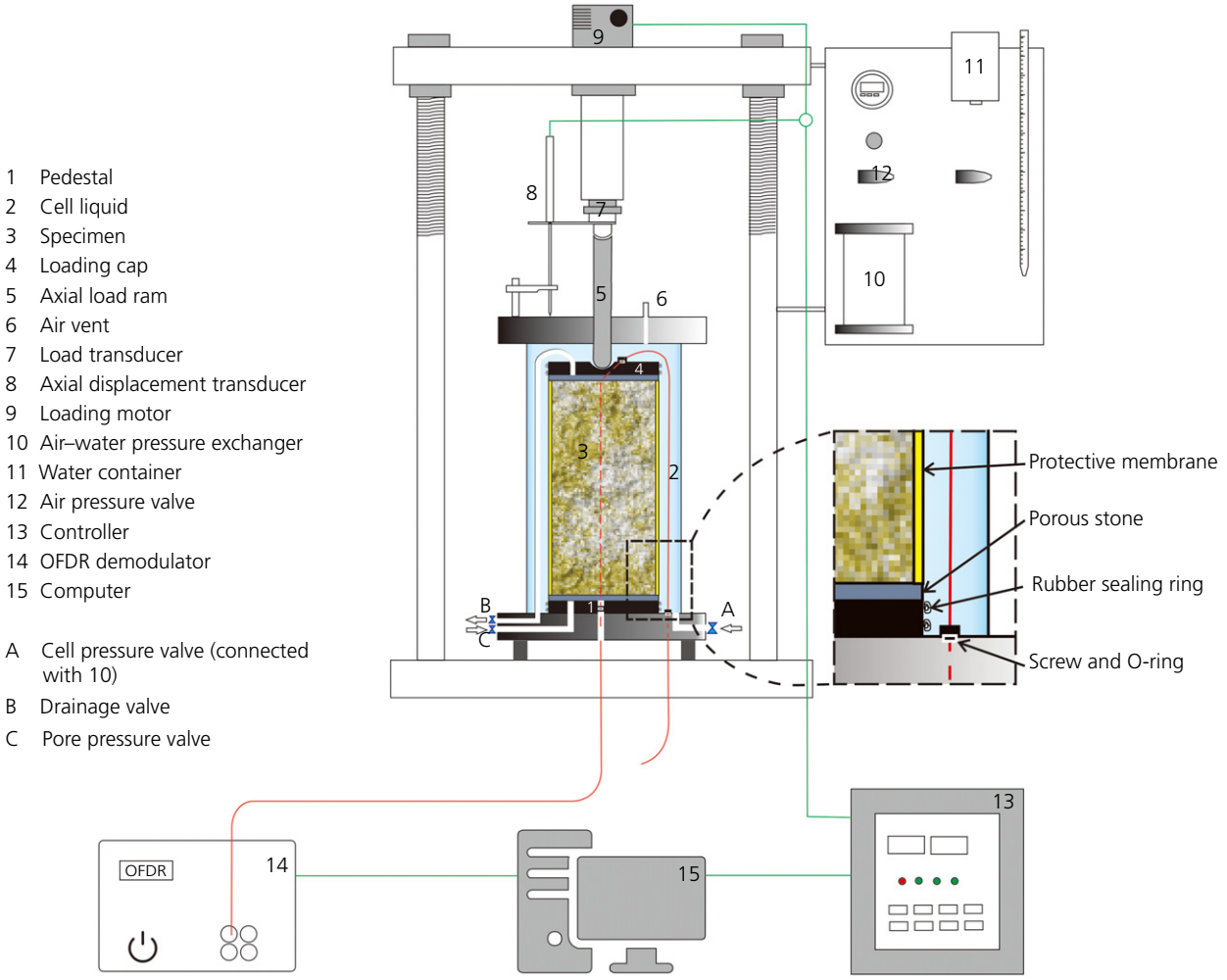


**Figure 4.** Diagram of the triaxial apparatus developed

the specimen measured by linear variable differential transducer (LVDT). The residual strain for $SS_d$ induced by plastic deformation is the largest, followed by $FS_d$, and the smallest is for $IS_d$. When the deviatoric stress is unloaded to 0 kPa, the residual strains in the middle of the $SS_d$, $FS_d$ and $IS_d$ specimens are 321, 120 and 0 με, respectively. The largest residual strain of $SS_d$ can be attributed to the fine particles' movement and filling of the gaps between the coarse particles under the compression condition because the coefficient $C_u$ of SS (Table 2) is the largest.

### 4.1.2 Results of the cyclic CD test on wet sand

The strain distributions of the optical fibre during the cyclic CD test on wet sand are shown in Figure 9. The test results of 500 kPa confining pressure are chosen for demonstration because the results under confining pressures of 200, 400 and 500 kPa are similar. The strains in the first loading–unloading cycle (C1) are larger than those in the next two cycles, C2 and C3, and the strains in C2 and C3 are basically the same. The dry specimens were relatively loose as a result of being prepared using the layered compaction method. The infiltrated specimens were basically compacted after experiencing one loading–unloading cycle. Similarly to the result of the CD test of the $SS_d$, the residual strain of the $SS_w$ was the largest in the cyclic CD test, followed by that of the $FS_w$, and the $IS_w$ was the smallest. Another point to note is that there is a noticeable disparity in strain at a height of 150 mm compared to that at −150 mm, as shown in Figure 9. This phenomenon can be ascribed to the constraining effect, which increases slightly from the top to the bottom of the specimen because of the weight of the sand and water.

## 4.2 Fitting of deformations integrated by fibre strain and obtained by LVDT

Based on the strain distributions of the optical fibre in Section 3.1, the average fibre strain ($\bar{\varepsilon_f}$) was calculated according to Equation 2. To eliminate the influence of the end effect on the integration results, the strains of the middle one-third specimen

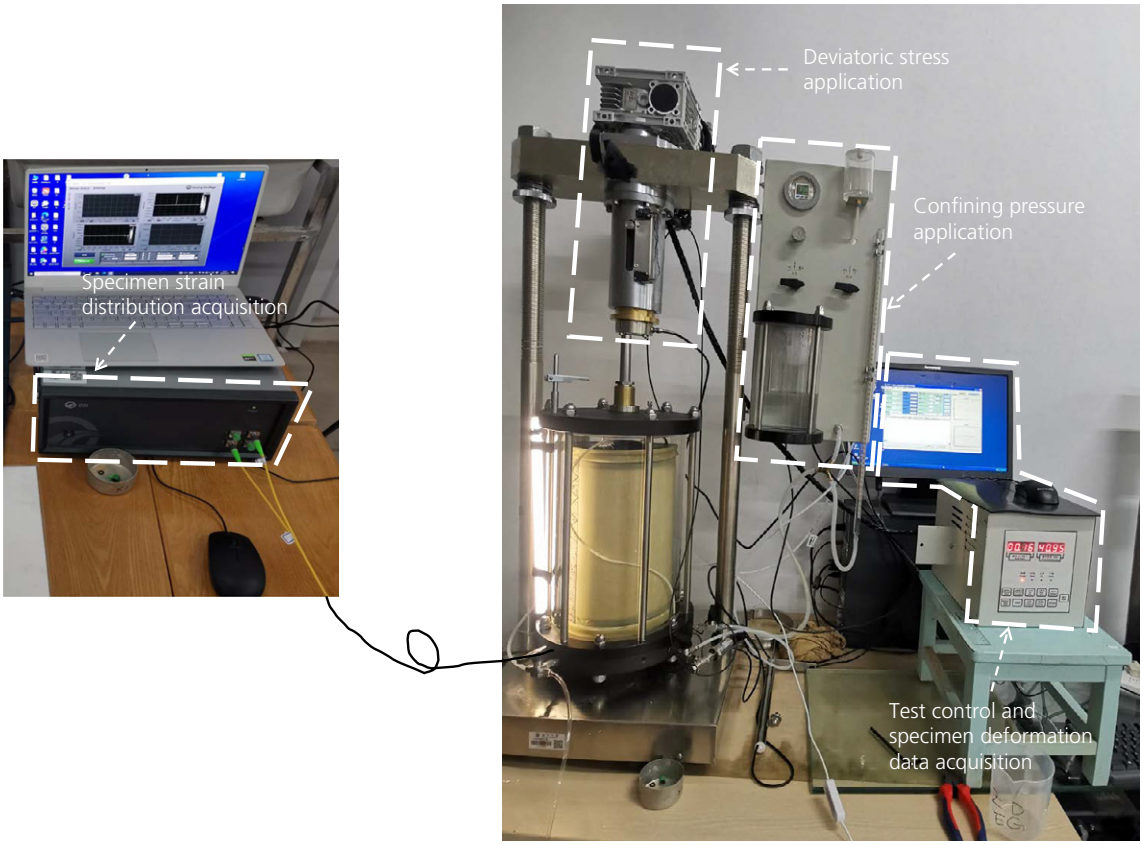


**Figure 5.** Photographs of the triaxial apparatus developed

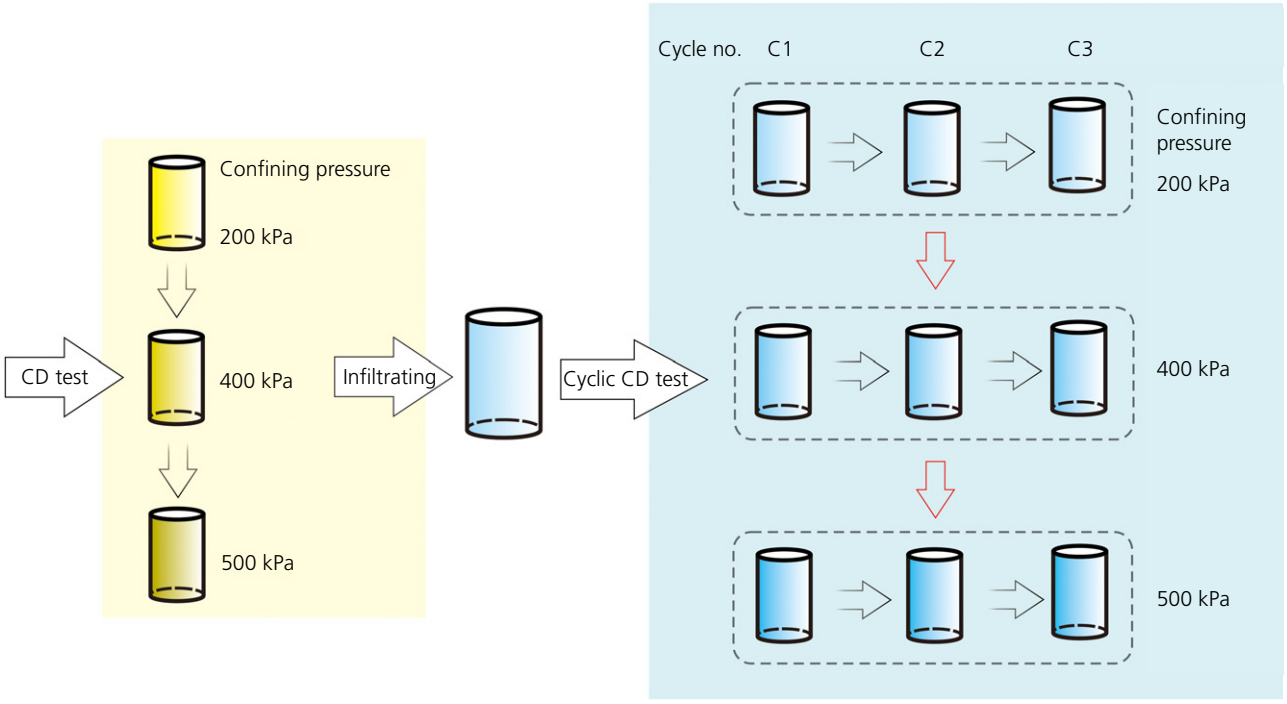


**Figure 6.** Test process undergone by a specimen

**Table 3.** Scheme of the CD test on dry specimens

| Sand | Specimen | Height: mm | Diameter: mm | Dry density: g/cm$^3$ | Confining pressure: kPa | Deviatoric stress: kPa |
|---|---|---|---|---|---|---|
| FS | $FS_d$ | 301 | 150 | 1.71 | 200 | 0, 25, 50, 75, 100 |
| IS | $IS_d$ | 302 | 150 | 1.6 | 400 | 0, 50, 100, 150, 200 |
| SS | $SS_d$ | 300 | 150 | 1.63 | 500 | 0, 50, 100, 150, 200, 250 |

**Table 4.** Scheme of the cyclic triaxial test on wet specimens

| Sand | Specimen | Water content: % | Number of loading-unloading cycles | Confining pressure: kPa | Deviatoric stress: kPa |
|---|---|---|---|---|---|
| FS | $FS_w$ | 8.09 | 3 | 200 | 0, 25, 50, 75, 100 |
| IS | $IS_w$ | 11.05 | 3 | 400 | 0, 50, 100, 150, 200 |
| SS | $SS_w$ | 11.24 | 3 | 500 | 0, 50, 100, 150, 200, 250 |

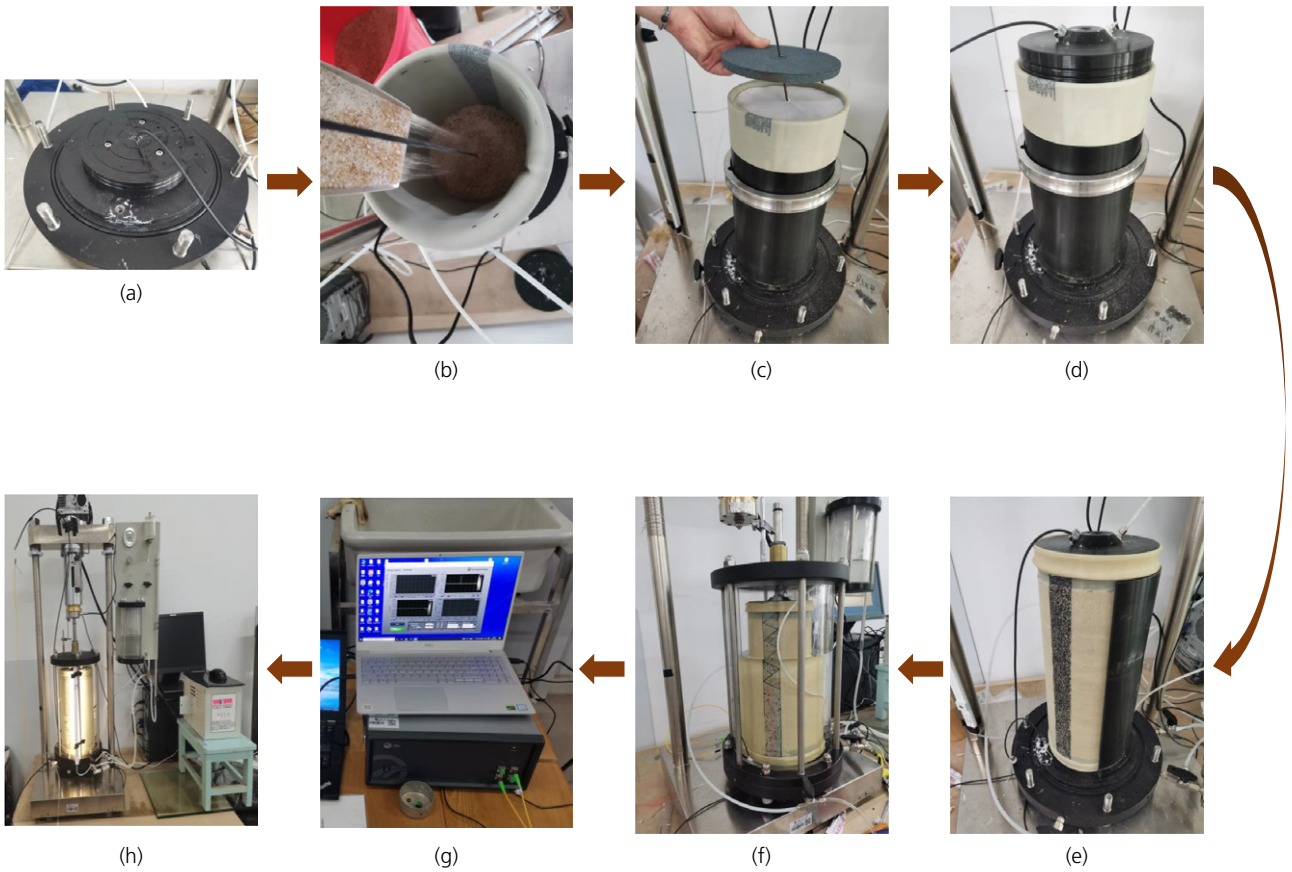


**Figure 7.** Main test procedures: (a) sensing cable is passed through; (b) mould is filled with sand and sensing cable is kept stretched during specimen preparation; (c) filter paper and porous stone are placed; (d) loading cap is put in place and screws are tightened where the sensing cable exits the specimen; (e) vacuum pressure is applied and split mould is dismantled; (f) triaxial cell is filled with water; (g) one end of sensing cable is connected with OFDR demodulator; (h) confining pressure and deviatoric stress are applied

section were taken to calculate $\bar{\varepsilon_f}$, so $L = 50$ mm and $d = 10$ mm in Equation 2. The deformation integrated by the strains of the optical fibre is rewritten as $d_f = 300\bar{\varepsilon_f}$. The axial deformation of the specimen ($d_s$) was measured directly using an LVDT during the test. A linear fitting is conducted between $d_f$ and $d_s$. The slope of the fitted line is defined as the $DC_{f\text{-}s}$ coefficient. Figures 10

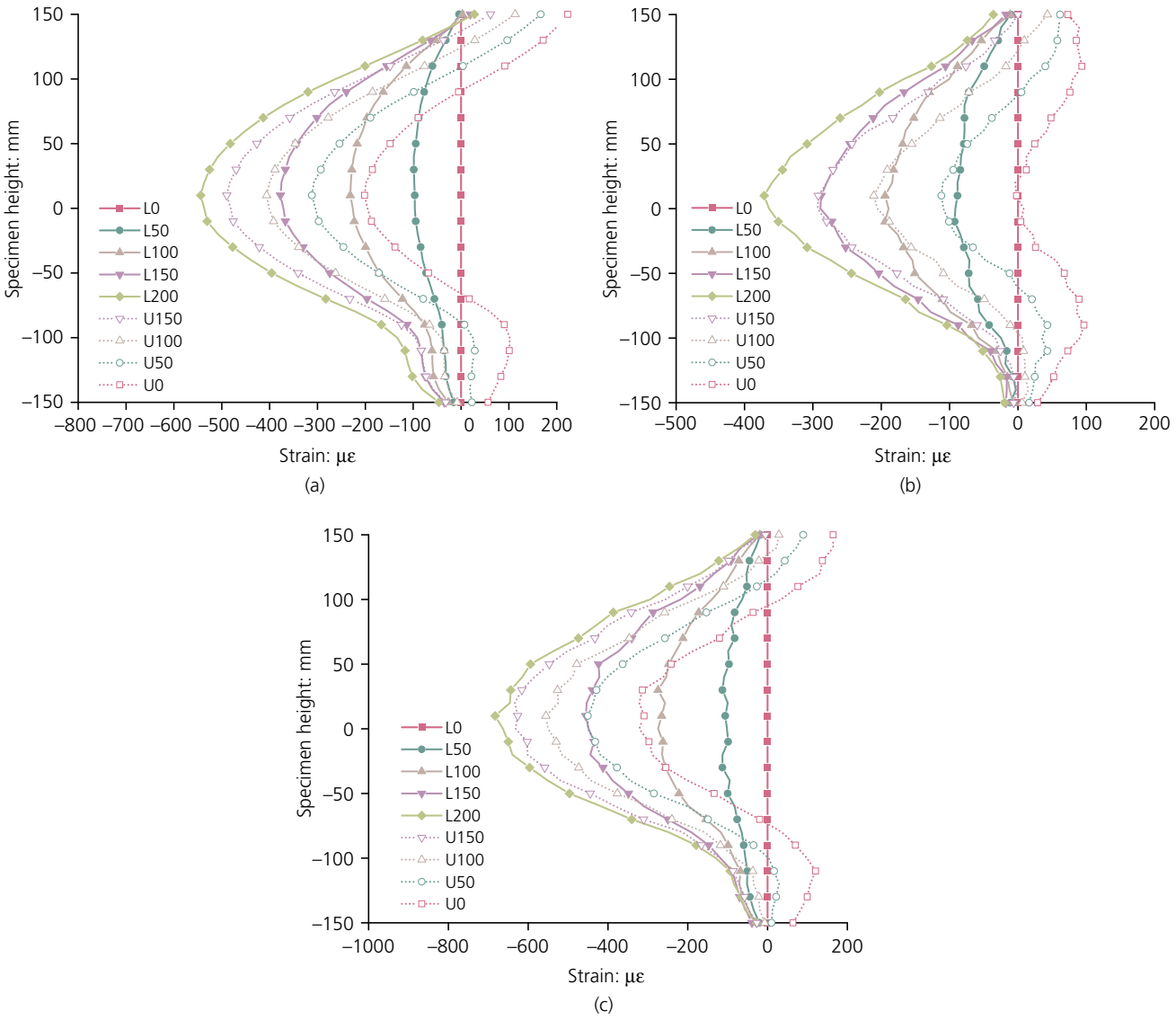


**Figure 8.** Strain distribution of the optical fibre during the CD test under a 400 kPa confining pressure: (a) specimen of $FS_d$; (b) specimen of $IS_d$; and (c) specimen of $SS_d$. The specimen height of 0 indicates the middle of the specimen. The solid lines with solid symbols correspond to the strain distribution during the loading process, and the dotted lines with hollow symbols show the strain distribution during the unloading process. 'L' and 'U' indicate loading and unloading, respectively. Numbers following 'L' and 'U' indicate the deviatoric stress

and 11 are the deformation fittings of $FS_d$ and $FS_w$, from which a good linear relationship between $d_f$ and $d_s$ is verified. The magnitude of the $DC_{f\text{-}s}$ coefficient is depicted in Figures 12 and 13. According to the definition of the $DC_{f\text{-}s}$ coefficient, the closer it is to 1, the better is the deformation coordination between the optical fibre and the soil. The differences and connections between the $DC_{f\text{-}s}$ coefficients under varied conditions reflect the influencing factors of $DC_{f\text{-}s}$. From the fitting results presented, a clear relationship can be observed between the $DC_{f\text{-}s}$ coefficient and various factors, including the type of soil, confining pressure, deviatoric stress and number of loading–unloading cycles. These influencing factors can be divided into two main categories with consideration of the environmental conditions for the practical application of DOFS in LS monitoring: (*a*) the properties of the borehole backfills, including particle size and gradation of the sand; (*b*) the site conditions, including the installation depth of the sensing cable, groundwater level and cyclic variation of the loads.

The particle sizes of the FS and IS are both uniform, and the average particle size of the IS is larger than that of the FS. Figure 12 illustrates that, under various confining pressures, the $DC_{f\text{-}s}$ coefficient of the FS consistently remains smaller than that of the IS. This observation suggests that the

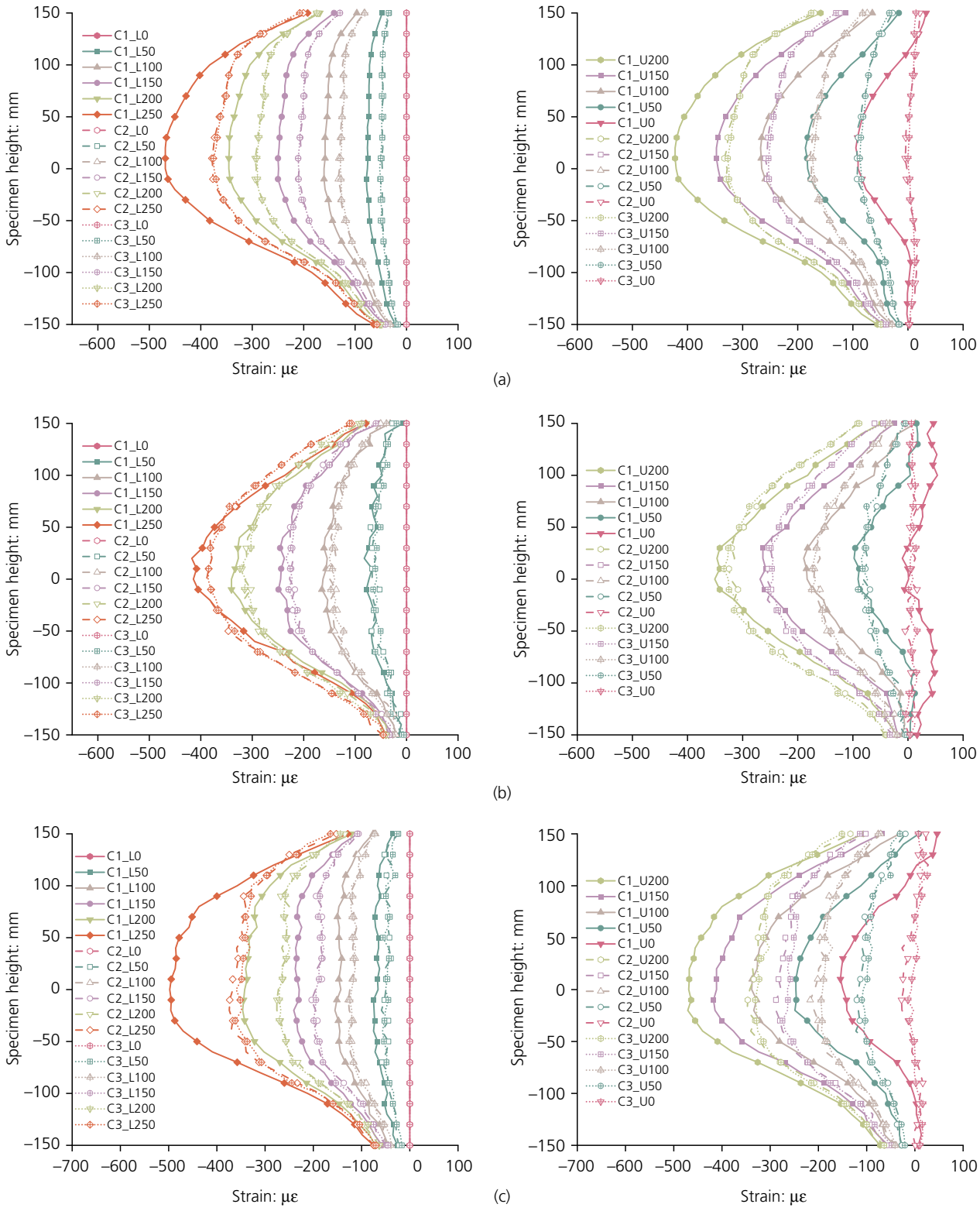


**Figure 9.** Strain distribution of the optical fibre during the cyclic CD test on: (a) specimen of $FS_w$, loading (left) and unloading (right); (b) specimen of $IS_w$, loading (left) and unloading (right); (c) specimen of $SS_w$, loading (left) and unloading (right). C1, C2 and C3 indicate cycle 1, cycle 2 and cycle 3, respectively. Every cycle includes the process of loading and unloading

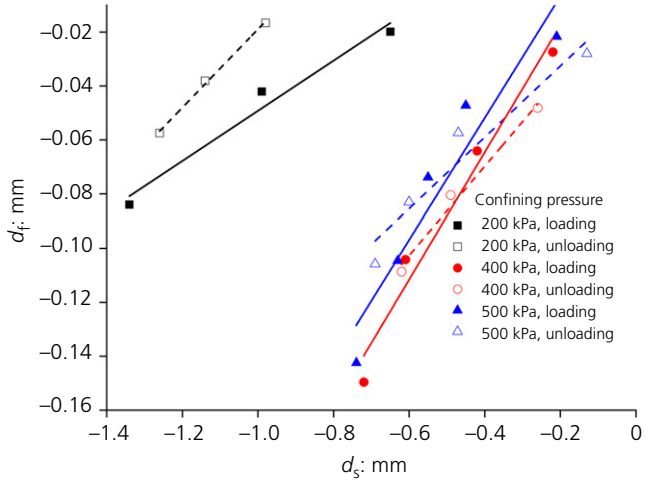


**Figure 10.** Deformation fitting of specimen of $FS_d$ under the CD test. $d_f$, deformation integrated by strains of the optical fibre; $d_s$, axial deformation of specimen obtained by LVDT

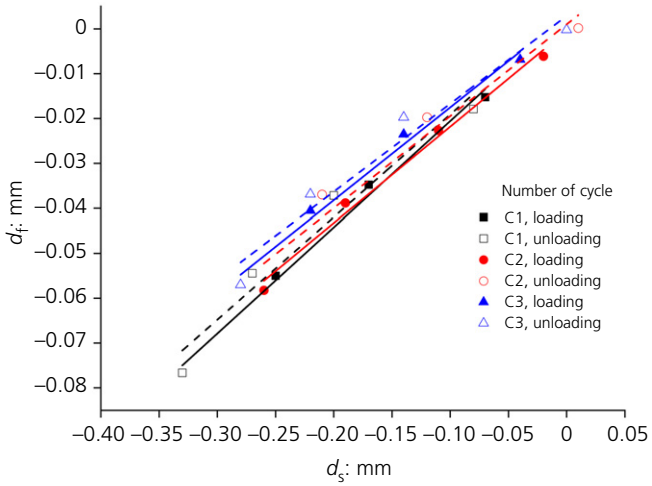


**Figure 11.** Deformation fitting of specimen of $FS_w$ under the cyclic CD test (confining pressure = 200 kPa). $d_f$, deformation integrated by strains of the optical fibre; $d_s$, axial deformation of specimen obtained by LVDT

utilisation of backfill sand with a larger particle size in the LS monitoring borehole contributes to an enhanced $DC_{f\text{-}s}$. In addition, the average particle sizes of the IS and the SS are close, and the $C_u$ of the SS is larger. From the data presented in Figure 12, it is evident that the $DC_{f\text{-}s}$ coefficient of IS is always larger than that of SS under consistent confining pressure, regardless of a CD test of the dry specimen or a cyclic CD test of the wet specimen, indicating that the poorly graded borehole backfills will be helpful to improve the $DC_{f\text{-}s}$.

According to Table 2, the average dry density of the three specimens is 1.65 g/cm$^3$ and their average friction angle is 25.16°. Therefore, the coefficient of lateral earth pressure $K_0$ is 0.57, and the underground depth corresponding to a confining pressure of

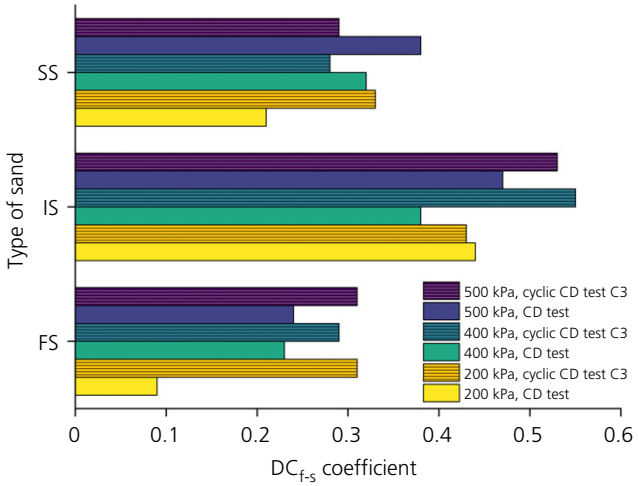


**Figure 12.** $DC_{f\text{-}s}$ coefficient of different types of sand under the loading condition of a CD test and a cyclic CD test with different confining pressures

200 kPa is approximately 22 m. Similarly, the corresponding depths of the confining pressures of 400 kPa and 500 kPa are approximately 44 m and 55 m, respectively. Different confining pressures correspond to various underground depths or installation depths of the sensing cable. From Figures 12 and 13, it can be observed that the $DC_{f\text{-}s}$ coefficient is smaller at a confining pressure of 200 kPa and generally increases with the confining pressure, regardless of whether a CD test or a cyclic CD test is performed. This shows that the $DC_{f\text{-}s}$ will be improved with the increasing installation depths of the sensing cable.

The CD test is conducted on a dry specimen, whereas the cyclic CD test is conducted on an infiltrated specimen. Water content is one of the main differences between the two test conditions. The $DC_{f\text{-}s}$ coefficient increases when the specimen is wet under the conditions of the same sand type and the same confining pressure (Figure 12), which indicates that a better $DC_{f\text{-}s}$ can be achieved if the sensing cable is installed below the groundwater table for practical LS monitoring.

The $DC_{f\text{-}s}$ coefficient at the first loading–unloading cycle (C1) is the largest, as shown in Figure 13. In the next two cycles, the $DC_{f\text{-}s}$ coefficient decreases slightly and tends to be stable. That is, cyclic variation of the loads also affects the $DC_{f\text{-}s}$. The loading–unloading cycles can be regarded as the compression and tensile deformation of the strata because of the variation of the water table during land subsidence. Therefore, the test results verify that DOFS is suitable for long-term soil deformation monitoring in LS, even if the water table changes periodically.

### 4.3 Discussion of the experimental and theoretical $DC_{f\text{-}s}$ coefficient

By establishing a fibre–soil interface strain transfer model, the quantitative relationship between the soil strain and the strain

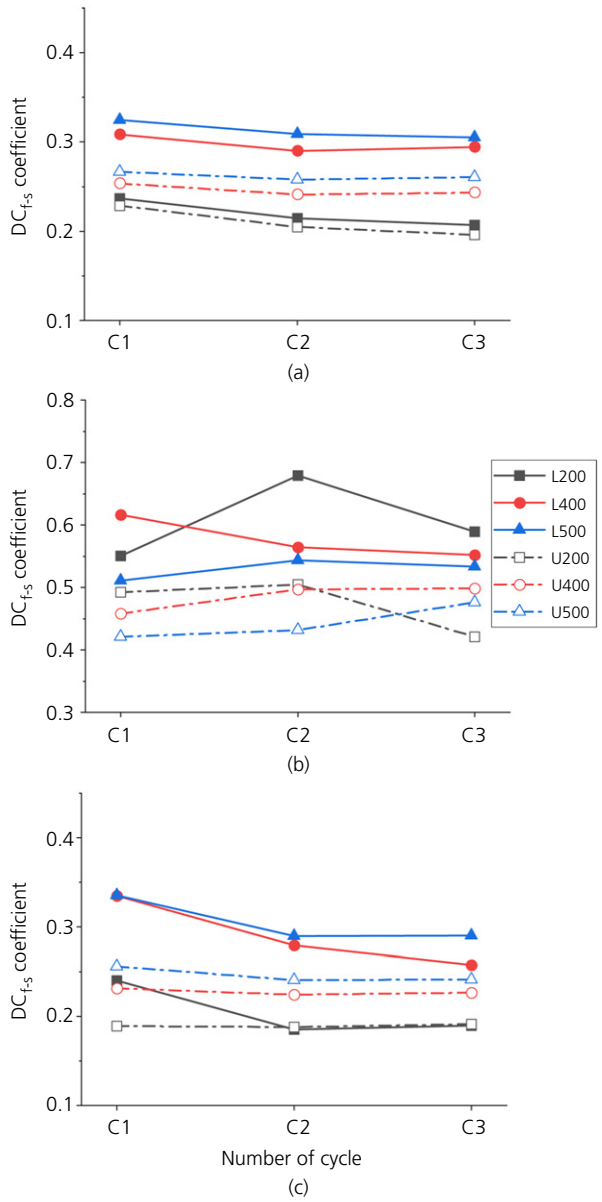


**Figure 13.** $DC_{f\text{-}s}$ coefficient for different times of the loading–unloading cycle: (a) specimen of $FS_w$; (b) specimen of $IS_w$; (c) specimen of $SS_w$

transferred to the fibre core was analysed, and then the fibre–soil strain transfer rate ($\alpha$) was calculated (Ansari and Yuan, 1998; Li *et al.*, 2012). The meaning of $\alpha$ and that of the $DC_{f\text{-}s}$ coefficient are the same. Based on previous theoretical models, Wu *et al.* (2022) found that the theoretical average fibre–soil strain transfer rate is 0.79. However, the experimental rates in their study were 0.5–0.65, and they considered slippage at the fibre–soil interface and confirmed the occurrence of relative slippage by theoretical derivation. It can be seen from Figure 13 that the experimental $DC_{f\text{-}s}$ coefficients of the FS and the SS are 0.2–0.35, and the $DC_{f\text{-}s}$ coefficients of the IS are 0.45–0.65. The experimental $DC_{f\text{-}s}$ coefficients are lower than the theoretical $DC_{f\text{-}s}$ coefficient. This could be explained by the large Young's modulus (Table 1) and thick jacket (Figure 2) of the Ø 5 mm MRC. For that reason, the strain transfer characteristic is more complex for the Ø 5 mm MRC sensing cable, and a relative slippage at the interface between the sensing cable and the soil is likely to occur.

The Ø 5 mm MRC, owing to its better sheath protection and higher tensile strength, is able to work continuously in harsh environments and has good practicality for engineering applications (Wu *et al.*, 2015). The deformation of the soil and that of the sensing cable have a good linear relationship, as shown in Figures 10 and 11, which indicates that the soil deformation can be calculated from the optical fibre strains if the $DC_{f\text{-}s}$ coefficient is obtained based on experiments under the same conditions.

## 5. Conclusions

Characteristics of the $DC_{f\text{-}s}$ under different conditions are critical issues for LS monitoring with DOFS, in which the optical sensing cable is installed in a borehole. The optical sensing cable directly contacts the borehole backfill materials instead of the original strata. The common backfills are sand soils, such as FS, IS and SS. A CD test on the dry sand and a cyclic CD test on the wet sand were carried out by modifying a traditional triaxial apparatus, and the $DC_{f\text{-}s}$ between the Ø 5 mm MRC sensing cable and three types of sand soils were tested. It was found that factors affecting $DC_{f\text{-}s}$ can be divided into two categories:

- properties of the borehole backfill materials – the larger and more uniform the particle size of the backfill is, the better is the $DC_{f\text{-}s}$
- site conditions – the deeper the installation depth of the sensing cable is, the better is the $DC_{f\text{-}s}$. The $DC_{f\text{-}s}$ values of wet sand are better than those of dry sand. The $DC_{f\text{-}s}$ tends to be stabilised for long-term LS monitoring.

Although the $DC_{f\text{-}s}$ coefficient obtained from the tests is lower than the theoretical values, the deformation of the fibre and the soil has a good linear relationship. Therefore, accurate measurement of the soil deformation can be achieved by calibrating the fibre strains based on the $DC_{f\text{-}s}$ coefficient.

## Competing interests statement

The authors declare there are no competing interests.

## Data availability statement

The data generated and analysed during this study are available on reasonable request to the corresponding author.

## Funding statement

This work was supported by the National Natural Science Foundation of China (no. 42077233), the Open Project of Key Laboratory of Earth Fissures Geological Disaster of the

Ministry of Land and Resources (no. JSDDY-HJ-D-2018-021), and the Natural Science Foundation of Jiangsu Province (no. SBK2023022563).

**REFERENCES**

Ansari F and Yuan LB (1998) Mechanics of bond and interface shear transfer in optical fiber sensors. *Journal of Engineering Mechanics* **124(4)**: 385–394, https://doi.org/10.1061/(ASCE)0733-9399(1998)124:4(385).

Bagheri-Gavkosh M, Hosseini SM, Ataie-Ashtiani B *et al.* (2021) Land subsidence: a global challenge. *Science of the Total Environment* **778**: article 146193, https://doi.org/10.1016/j.scitotenv.2021.146193.

Barrias A, Casas JR and Villalba S (2016) A review of distributed optical fiber sensors for civil engineering applications. *Sensors* **16(5)**: article 748, https://doi.org/10.3390/s16050748.

Chen Y and Zhang D (2011) *The Pullout Test to Study the Interface Effect Between the Optical Sensing Fiber and the Soil*. Nanjing University, Nanjing, China. See https://ssrn.com/abstract=4293178 (accessed 30/08/2023).

Galloway DL and Burbey TJ (2011) Review: regional land subsidence accompanying groundwater extraction. *Hydrogeology Journal* **19(8)**: 1459–1486, https://doi.org/10.1007/s10040-011-0775-5.

Henault JM, Salin J, Moreau G *et al.* (2011) Monitoring of concrete structures using OFDR technique. *AIP Conference Proceedings* **1335(1)**: 1386–1393, https://doi.org/10.1063/1.3592094.

Her SC and Huang CY (2011) Effect of coating on the strain transfer of optical fiber sensors. *Sensors* **11(7)**: 6926–6941, https://doi.org/10.3390/s110706926.

Herrera-García G, Ezquerro P, Tomás R *et al.* (2021) Mapping the global threat of land subsidence. *Science* **371(6524)**: 34–36, https://doi.org/10.1126/science.abb85.

Leung CKY, Wan KT, Inaudi D *et al.* (2015) Review: optical fiber sensors for civil engineering applications. *Materials and Structures* **48(4)**: 871–906, https://doi.org/10.1617/s11527-013-0201-7.

Li DS, Ren L and Li HN (2012) Mechanical property and strain transferring mechanism in optical fiber sensors. In *Fiber Optic Sensors* (Yasin M, Harun SW and Arof H (eds)). IntechOpen, London, UK, pp. 439–451, https://doi.org/10.5772/27731.

Liu C, Shi B, Gu K *et al.* (2022) Negative pore water pressure in aquitard enhances land subsidence: field, laboratory, and numerical evidence. *Water Resources Research* **58(1)**: article e2021WR030085, https://doi.org/10.1029/2021WR030085.

Shirzaei M, Freymueller J, Törnqvist TE *et al.* (2021) Measuring, modelling and projecting coastal land subsidence. *Nature Reviews Earth & Environment* **2(1)**: 40–58, https://doi.org/10.1038/s43017-020-00115-x.

Wang YQ, Wang ZF and Cheng WC (2019) A review on land subsidence caused by groundwater withdrawal in Xi'an, China. *Bulletin of Engineering Geology and the Environment* **78(4)**: 2851–2863, https://doi.org/10.1007/s10064-018-1278-6.

Wu JC, Shi XQ, Xue YQ *et al.* (2008) The development and control of the land subsidence in the Yangtze Delta, China. *Environmental Geology* **55(8)**: 1725–1735, https://doi.org/10.1007/s00254-007-1123-x.

Wu JH, Jiang HT, Su JW *et al.* (2015) Application of distributed fiber optic sensing technique in land subsidence monitoring. *Journal of Civil Structural Health Monitoring* **5(5)**: 587–597, https://doi.org/10.1007/s13349-015-0133-8.

Wu H, Zhu HH, Zhang CC *et al.* (2020) Strain integration-based soil shear displacement measurement using high-resolution strain sensing technology. *Measurement* **166**: article 108210, https://doi.org/10.1016/j.measurement.2020.108210.

Wu GZ, Zhang D, Shan TS *et al.* (2022) Characterizing the strain transfer on the sensing cable-soil interface based on triaxial testing. *Smart Structures and Systems* **30(1)**: 63–74, https://doi.org/10.12989/sss.2022.30.1.063.

Xu YS, Ma L, Du YJ and Shen SL (2012) Analysis of urbanisation-induced land subsidence in Shanghai. *Natural Hazards* **63(2)**: 1255–1267, https://doi.org/10.1007/s11069-012-0220-7.

Yang J, Sze HY and Heung MK (2009) Effect of initial static shear on cyclic behavior of sand. In *Proceedings of the 17th International Conference on Soil Mechanics and Geotechnical Engineering, Alexandria, Egypt* (Hamza M, Shahien M and El-Mossallamy Y (eds)). IOS Press, Amsterdam, the Netherlands, vols 1–4, pp. 155–158.

Yuan LB, Zhou LM and Wu JS (2001) Investigation of a coated optical fiber strain sensor embedded in a linear strain matrix material. *Optics and Lasers in Engineering* **35(4)**: 251–260, https://doi.org/10.1016/S0143-8166(01)00007-0.

Zhang CC, Zhu HH, She JK, Zhang D and Shi B (2015) Quantitative evaluation of optical fiber/soil interfacial behavior and its implications for sensing fiber selection. *IEEE Sensors Journal* **15(5)**: 3059–3067, https://doi.org/10.1109/JSEN.2014.2386881.

Zhang CC, Shi B, Gu K *et al.* (2018) Vertically distributed sensing of deformation using fiber optic sensing. *Geophysical Research Letters* **45(21)**: 11732–11741, https://doi.org/10.1029/2018GL080428.